https://doi.org/10.2352/ISSN.2470-1173.2019.13.COIMG-133

Joint Density Map and Continuous Angular Refinement in Cryo-Electron Microscopy

Mona Zehni [1], *Laurène Donati* [2], *Emmanuel Soubies* [2], *Zhizhen J. Zhao* [1], *Minh N. Do* [1], *Michael Unser* [2]
[1] *Coordinate Science Laboratory, University of Illinois at Urbana-Champaign*
[2] *Biomedical Imaging Group, École Polytechnique Fédérale de Lausanne (EPFL)*

Abstract

Cryo-electron microscopy (Cryo-EM) is a popular imaging modality used to visualize a wide range of bio-molecules in their 3D form. The goal in Cryo-EM is to reconstruct the 3D density map of a molecule from projection images taken from random and unknown orientations. A critical step in the Cryo-EM pipeline is 3D refinement. In this procedure, an initial 3D map and a set of estimated projection orientations is refined to obtain higher resolution maps. State-of-the-art refinement techniques rely on projection matching steps in order to refine the initial projection orientations. Unfortunately projection matching is computationally inefficient and it requires a finite discretization of the space of orientations. To avoid repeated projection matching steps, in this work we consider the orientation variables in their continuous form. This enables us to formulate the refinement problem as a joint optimization problem that refines the underlying density map and orientations. We use alternating direction method of multipliers (ADMM) and gradient descent steps in order to update the density map and the orientations, respectively. Our results and their comparison with several baselines demonstrate the feasibility and performance of the proposed refinement framework.

Introduction

Revealing the 3D structure of biological molecules is motivated by better diagnosis of disease, more efficient medicine design and the gain of a deeper understanding of how biological processes take place. Cryo-EM is an imaging modality that has gained popularity over the recent decades for its ability to visualize the 3D structure of various molecules [1].

In Cryo-EM, samples of the same molecule are frozen at cryogenic temperature and then imaged by a transmission electron microscope (TEM). Each sample of the molecule is frozen in a random unknown 3D orientation with respect to the parallel electron beams. Thus, the X-ray transform of the molecule from random unknown 3D orientations is captured on the detector in the form of particle images. Single particle analysis (SPA) then targets recovering the 3D density map of the molecule from hundreds to thousands of projection images.

The reconstruction of the density map involves 3D ab-initio modeling and 3D refinement [2]. Ab-initio modeling targets the template-free reconstruction of a 3D map from the particle images [3]. The output of the ab-initio model only captures coarse characteristics of the underlying density map. Then the refinement step refines the initial map alongside with initial estimates of the unknown 3D orientations (poses) of the particle images in order to achieve a higher resolution density map.

Various methods target the joint reconstruction of the density map and the 3D pose variables. In iterative projection matching, joint reconstruction is performed through alternating steps of template matching for updating 3D orientations and density map reconstruction [6]. The problem can also be viewed in a Baysian framework and formulated as a maximum a posteriori (MAP) estimation problem [5, 7], which is then solved through expectation maximization (EM) or stochastic gradient descent. Although iterative projection matching and Baysian frameworks formulate the problem differently, the way the 3D projection orientations are updated in both frameworks requires some form of template matching. This implies that 1) a discretization of the projection orientations is required to obtain a finite number of templates to compare each particle image against, 2) repeated template matching steps are required at each iteration of the joint reconstruction process to update the projection orientations.

To avoid these drawbacks, we consider the 3D pose variables in their continuous form. We then formulate the refinement process as a joint optimization problem between the density map and the 3D poses. This problem is then solved by alternating minimization. We update the density map and projection orientations via alternating direction method of multipliers (ADMM) and gradient descent (GD) steps, respectively. Our results demonstrate the feasibility of this method in refining the initial map and the initial orientations.

System model

We formulate the Cryo-EM forward model as,

$$\mathrm{g}_\ell[\mathbf{m}] = (h * \mathscr{P}_{\boldsymbol{\theta}_\ell}(V))[\boldsymbol{\Lambda}\mathbf{m}] + \varepsilon_\ell[\mathbf{m}], \quad \ell \in \{1,\dots,L\}, \qquad (1)$$

where $V : \mathscr{L}(\mathbb{R}^3) \to \mathbb{R}$ denotes the density map and $\mathbf{g}_\ell$ is the ℓ-th discretized projection image in the set of L projection images. The operator $\mathscr{P}_{\boldsymbol{\theta}} : \mathscr{L}(\mathbb{R}^3) \to \mathscr{L}(\mathbb{R}^2)$ describes the X-ray transform operator that acts along the direction $\boldsymbol{\theta}$. Note that $\boldsymbol{\theta}_\ell = (\theta_{\ell,1}, \theta_{\ell,2}, \theta_{\ell,3})$ is the Euler representation of the orientation vector corresponding to the ℓ-th projection image where $\theta_{\ell,1}$, $\theta_{\ell,2}$ and $\theta_{\ell,3}$ denote the rotation, tilt and in-plane rotation respectively. The point spread function (PSF) $h \in \mathscr{L}(\mathbb{R}^2)$ models the effects of the microscope as contrast transfer function (CTF). Finally, uniformly-spaced samples of projected density map are detected such that $\boldsymbol{\Lambda} = \mathrm{diag}[\Lambda_x, \Lambda_y]$ and $\mathbf{m} \in \Omega \subset \mathbb{Z}^2$. In addition, each pixel of the ℓ-th projection image is contaminated by i.i.d. Gaussian noise $\varepsilon_\ell[\mathbf{m}] \sim \mathscr{N}(0, \sigma^2)$ with zero mean and σ^2 variance.

This research is partially supported by the European Research Council (ERC) under the European Union's Horizon 2020 research and innovation programme, GrantAgreement No. 692726 GlobalBioIm: Global integrative framework for computational bio-imaging.

In (1), the X-ray transform operator acts in the continuous domain. Thus, following [8], we discretize the forward operator and further represent it by a finite-dimensional matrix by expanding the density map onto the shift invariant space,

$$V(\mathbf{x}) = \sum_{\mathbf{k}\in\mathbb{Z}^3} \mathrm{c}[\mathbf{k}]\varphi(\mathbf{x}-\mathbf{k}), \tag{2}$$

where c is the discrete representation of V within the basis $\{\varphi(\cdot-\mathbf{k})\}_{\mathbf{k}\in\mathbb{Z}^3}$. Here, similar to [8, 9], we choose the Kaiser-Bessel window functions (KBWF) for φ. Several properties of KBWF such as 1) compact support, 2) isotropy and 3) availability of closed-form expressions for their X-ray transforms [10] make them a particularly suitable choice. After, substituting (2) in (1), and using the pseudo-shift invariant property of X-ray transform [11], we have

$$\mathrm{g}_\ell[\mathbf{m}] = \sum_{\mathbf{k}\in\mathbb{Z}^3} \mathrm{c}[\mathbf{k}]\left(h * \mathscr{P}_{\boldsymbol{\theta}_\ell}(\varphi)\right)[\boldsymbol{\Lambda}\mathbf{m} - \mathbf{M}_{\boldsymbol{\theta}_\ell^\perp}\mathbf{k}] + \varepsilon_\ell[\mathbf{m}], \tag{3}$$

where, for a given $\boldsymbol{\theta}$,

$$\mathbf{M}_{\boldsymbol{\theta}^\perp} = \begin{bmatrix} c_1c_2c_3 - s_1s_3 & c_3s_1 + c_1c_2s_3 & -c_1s_2 \\ -c_1s_3 - c_2c_3s_1 & c_1c_3 - c_2s_1s_3 & s_1s_2 \end{bmatrix}. \tag{4}$$

The two rows of $\mathbf{M}_{\boldsymbol{\theta}^\perp}$ mark the orthonormal basis vectors in the projection plane where $c_i = \cos\theta_i$ and $s_i = \sin\theta_i$. Because the molecule is compactly supported, only a finite number of coefficients $\mathrm{c}[\mathbf{k}]$ are non-zeros and we can write (3) as

$$\mathbf{g}_\ell = \mathbf{H}_\ell\mathbf{c} + \boldsymbol{\varepsilon}, \tag{5}$$

where $\mathbf{H}_\ell$ is a matrix whose entries are given by

$$[\mathbf{H}_\ell]_{\mathbf{m},\mathbf{k}} = \left(h * \mathscr{P}_{\boldsymbol{\theta}_\ell}(\varphi)\right)[\boldsymbol{\Lambda}\mathbf{m} - \mathbf{M}_{\boldsymbol{\theta}_\ell^\perp}\mathbf{k}]. \tag{6}$$

Finally, by stacking all the projection images and their corresponding matrix-vector product form we get

$$\mathbf{g} = \mathbf{H}(\boldsymbol{\Theta})\,\mathbf{c}, \tag{7}$$

where $\mathbf{g} = [\mathbf{g}_1^T \cdots \mathbf{g}_L^T]^T$, $\mathbf{H}(\boldsymbol{\Theta}) = [\mathbf{H}_1^T \cdots \mathbf{H}_L^T]^T$ and $\boldsymbol{\Theta} = \{\boldsymbol{\theta}_\ell\}_{\ell=1}^L$.

Problem formulation

Based on (7), the joint refinement of the density map and 3D pose variables is written as

$$(\widehat{\mathbf{c}}, \widehat{\boldsymbol{\Theta}}) \in \left\{ \arg\min_{\mathbf{c},\boldsymbol{\Theta}} J(\boldsymbol{\Theta}, \mathbf{c}) \right\}, \tag{8}$$

where

$$J(\boldsymbol{\Theta}, \mathbf{c}) = \frac{1}{2}\|\mathbf{g} - \mathbf{H}(\boldsymbol{\Theta})\,\mathbf{c}\|^2 + \lambda\,\|\boldsymbol{\nabla}\mathbf{c}\|_{2,1}. \tag{9}$$

The first term in (9) corresponds to the data fidelity term, $\boldsymbol{\nabla}$ is the gradient operator, $\|\boldsymbol{\nabla}\cdot\|_{2,1}$ corresponds to the total variation (TV) regularizer [12], and $\lambda > 0$ is the regularization weight. We propose to solve this challenging optimization problem using alternating minimization. Given the current estimation of the latent variables $\boldsymbol{\Theta}$, we take benefit from the convexity of $J(\cdot,\boldsymbol{\Theta})$ and update the density map using ADMM, as proposed in [8]. In contrast, when fixing the density map $\mathbf{c}$, $J(\mathbf{c},\cdot)$ is non-convex but differentiable. Hence, the latent variables are updated with a gradient descent. The outline of the proposed approach is summarized in Algorithm 1.

Algorithm 1 Joint Optimization Framework

procedure JOINT OPTIMIZATION($\mathbf{c}^0$,$\boldsymbol{\Theta}^0$)
  $k = 0$
  while $k < K_{\max}$ **do**
    Update the density map
    $\mathbf{c}^{k+1} \leftarrow \texttt{ADMM}\left(J(\cdot,\boldsymbol{\Theta}^k), \mathbf{c}^k\right)$
    Update the latent variables
    $\boldsymbol{\Theta}^{k+1} \leftarrow \texttt{GD}\left(J(\mathbf{c}^{k+1},\cdot), \boldsymbol{\Theta}^k\right)$
    $k \leftarrow k+1$
  end while
  return $\mathbf{c}^{K_{\max}}, \boldsymbol{\Theta}^{K_{\max}}$
end procedure

In Algorithm 1, $K_{\max}$ denotes the number of refinement iterations, $\texttt{ADMM}(J(\cdot,\boldsymbol{\Theta}^k), \mathbf{c}^k)$ refers to the minimization of $J(\cdot,\boldsymbol{\Theta}^k)$ using ADMM initialized with $\mathbf{c}^k$, and similarly for $\texttt{GD}(J(\mathbf{c}^{k+1},\cdot), \boldsymbol{\Theta}^k)$. Finally, Algorithm 1 is implemented within the framework of the GlobalBioIm Library [4].

Experiments

We use as ground truth, the human patched 1 (PTCH1) protein [13] from protein data bank (PDB) and generate $L = 500$ synthetic projection images according to (1). To initialize $\mathbf{c}$, we start from a coarse low-pass filtered version of the density map and extract its discretized representation as $\mathbf{c}^0$. To initialize the 3D pose variables, we add a Gaussian noise with zero mean and a standard deviation of $\sigma_\theta = 0.5$ Radians to each Euler angle in $\boldsymbol{\Theta}^{\text{true}}$ that has been used in the simulation. In other words, $\boldsymbol{\theta}_\ell^0 = \boldsymbol{\theta}_\ell^{\text{true}} + \boldsymbol{\varepsilon}_\ell$ where $\boldsymbol{\varepsilon}_\ell \sim \mathscr{N}(\mathbf{0}_3, \sigma_\theta\mathbf{I}_3)$ and $\boldsymbol{\Theta}^0 = \{\boldsymbol{\theta}_\ell^0\}_{\ell=1}^L$. Note that $\mathbf{0}_3$ represents a vector of zeros of length 3 and $\mathbf{I}_3$ is the identity matrix of size 3×3. In our experiments, we also used several functions provided by the Aspire package [16].

To assess the performance of our framework, we use the Fourier shell correlation (FSC) measure between the true (V^{true}) and the reconstructed volume ($\widehat{V}$) [14]. FSC captures the correlation between different Fourier frequency shells of the two density maps. Higher FSC in higher frequency shells indicates resemblance in small details between the two maps.

We also evaluate the quality of the 3D pose refinement by finding the correlation between the true and the refined pose vectors. We define the pose vector corresponding to the ℓ-th projection image based on the rotation and tilt angles as $\mathbf{p}_\ell = [\sin\theta_{\ell,2}\cos\theta_{\ell,1}, \sin\theta_{\ell,2}\sin\theta_{\ell,1}, \cos\theta_{\ell,1}]^T$. Based on this definition, the quantity $\langle \mathbf{p}_\ell^{\text{true}}, \widehat{\mathbf{p}}_\ell \rangle$ measures the correlation between the true and the refined pose vector for the ℓ-th projection image. A value of one (highest correlation) means that the two pose vectors are perfectly aligned. Similarly, to quantify the refinement of the in-plane rotations, we define $\mathbf{r}_\ell = [\cos\theta_{\ell,3}, \sin\theta_{\ell,3}]^T$ and we analyse the quantity $\langle \mathbf{r}_\ell^{\text{true}}, \widehat{\mathbf{r}}_\ell \rangle$.

Visual comparison Figure 1 shows the results of our approach with those of several baselines. The failed reconstruction in (c) shows that the initial 3D pose variables $\boldsymbol{\Theta}^0$ are far from their true values. On the other hand comparing our results (d) to (e) reveals that our approach is able to refine the initial map in (b) and

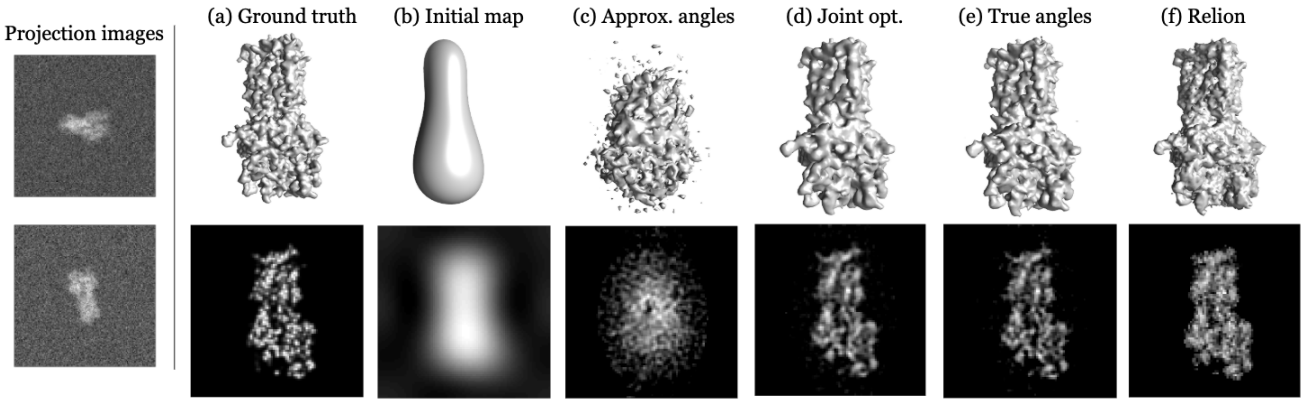

Figure 1. *Visual comparison between the refined density map and several baselines. The first column illustrates samples of the synthesized projection image with an average $SNR = 3.5781dB$. The first row (a)-(f) presents the density maps visualized in Chimera [15] and the second row shows the central slice of the map. The illustrated volumes are (a) the ground truth, (b) the initial map corresponding to $\mathbf{c}^0$, (c) the reconstructed density map obtained by solving (8) with respect to $\mathbf{c}$ assuming $\boldsymbol{\Theta} = \boldsymbol{\Theta}^0$, (d) our joint framework, (e) the reconstructed density map obtained by solving (8) with respect to $\mathbf{c}$ assuming perfect knowledge of the 3D pose variables, i.e. $\boldsymbol{\Theta} = \boldsymbol{\Theta}^{\text{true}}$, (f) Relion reconstruction [5].*

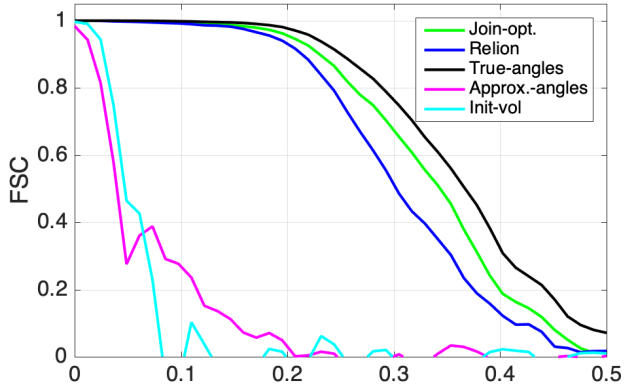

Figure 2. *Comparison between the FSC of the true density map and the baseline maps presented in Fig. 1.*

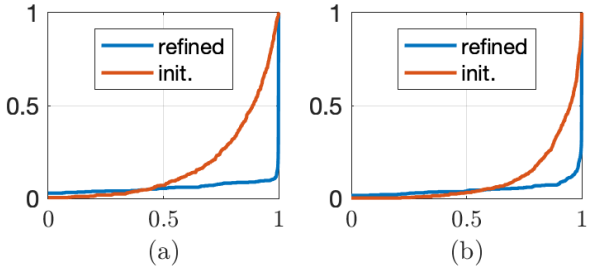

Figure 3. *CDF of the correlation between (a) the true and refined orientation vectors (blue curves), the true and the initial orientation vectors (red curves), (b) the true and refined rotation vectors (blue curves), the true and the initial rotation vectors (red curves).*

the initial 3D pose variable well. Finally, comparing (d) with (f), which is the result of the state of the art method for Cryo-EM 3D refinement, once again verifies the feasibility of our refinement approach.

FSC comparison. Figure 2 compares the FSC of the reconstructed map with the baseline maps presented in Figure 1. The results show that without refinement, the correlation between the true and the reconstructed map is very small (magenta curve). On the other hand, the FSC curve corresponding to our method (green curve) is reasonably close to the FSC of the baseline with perfect knowledge of the 3D pose variables (black curve) and Relion results (blue curve). The results obtained with Relion are inferior compared to the ones obtained by our method, which is worth noting.

Poses comparison We compare the cumulative distribution function (CDF) of $\{\langle \mathbf{p}_\ell^{\text{true}}, \widehat{\mathbf{p}}_\ell \rangle\}_{\ell=1}^L$ and $\{\langle \mathbf{r}_\ell^{\text{true}}, \widehat{\mathbf{r}}_\ell \rangle\}_{\ell=1}^L$ (blue curves) with $\{\langle \mathbf{p}_\ell^{\text{true}}, \mathbf{p}_\ell^0 \rangle\}_{\ell=1}^L$ and $\{\langle \mathbf{r}_\ell^{\text{true}}, \mathbf{r}_\ell^0 \rangle\}_{\ell=1}^L$ (red curves) in Figure 3. Note that $\{\mathbf{p}_\ell^0, \mathbf{r}_\ell^0\}_{\ell=1}^L$ are derived based on the initial 3D poses $\boldsymbol{\Theta}^0$. The results show that compared to $\{\langle \mathbf{p}_\ell^{\text{true}}, \mathbf{p}_\ell^0 \rangle\}_{\ell=1}^L$, $\{\langle \mathbf{p}_\ell^{\text{true}}, \widehat{\mathbf{p}}_\ell \rangle\}_{\ell=1}^L$ is more concentrated around one (except for a few outliers). This implies the successful refinement of the 3D pose variables for most projection images. The same also holds for $\{\langle \mathbf{r}_\ell, \widehat{\mathbf{r}}_\ell \rangle\}_{\ell=1}^L$ and its comparison with $\{\langle \mathbf{r}_\ell, \mathbf{r}_\ell^0 \rangle\}_{\ell=1}^L$. Note that the existence of outliers is explained by the non-convexity of the problem and getting stuck at local minima while optimizing for the 3D pose variables of some projection images.

In addition, Figure 4 depicts the CDF of the differences between 1) the true and initial angles (red curve), 2) the true and the refined angles (blue curve). The results show that while the initial error on the angles is mainly in the range of $[-40, 40]$ degrees, our refinement framework manages to refine the angles such that the final errors are mainly concentrated around zero.

Conclusion

In this paper, we proposed a framework for joint refinement of the density map and 3D pose variables in Cryo-EM. We used alternating steps in order to update the density map and the 3D pose variables. ADMM steps are used for the update of the density map. Unlike state of the art refinement methods that use projection matching in order to update 3D poses, we consider these variables in their continuous form. We then used gradient de-

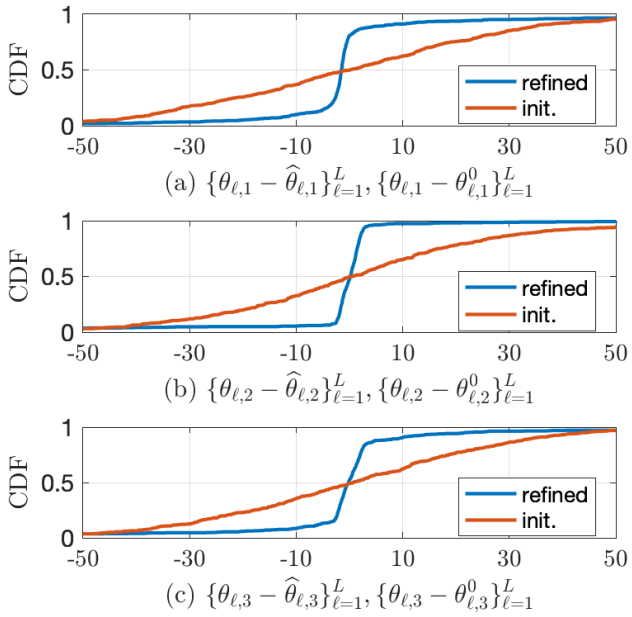

Figure 4. *CDF of the differences between the true and refined angles (blue curves), the true and the initial angles (red curves).*

scent steps to update these variables. Our experimental results and the comparison with several baselines demonstrated the feasibility and accuracy of our framework.

References

[1] Y. Cheng, N. Grigorieff, P. A. Penczek and T. Walz, A primer to single-particle cryo-electron microscopy, Cell, 161, 3 (2015).

[2] S. H W. Scheres, A Bayesian view on cryo-EM structure determination, J. of molecular biology, 415, 2 (2012).

[3] E. Levin, T. Bendory, N. Boumal, J. Kileel and A. Singer, 3D ab initio modeling in cryo-EM by autocorrelation analysis, ISBI, pg. 1569-1573. (2018).

[4] M. Unser, E. Soubies, F. Soulez, M. McCann, and L. Donati, A Unifying Computational Framework for Solving Inverse Problems, Proc. OSA Imaging and Applied Optics Congress on Computational Optical Sensing and Imaging (COSI'17), (2017).

[5] S. H.W. Scheres, RELION: Implementation of a Bayesian approach to cryo-EM structure determination, J. Structural Biology, 180, 3 (2012).

[6] Y. Michels, E. Baudrier and L. Mazo, Radial Function Based Ab-Initio Tomographic Reconstruction for Cryo Electron Microscopy, Proc. ICIP, (2018).

[7] A. Punjani, M. A. Brubaker and D. J. Fleet, Building Proteins in a Day: Efficient 3D Molecular Structure Estimation with Electron Cryo microscopy, IEEE Transactions on Pattern Analysis and Machine Intelligence, 39, 4 (2017).

[8] L. Donati, M. Nilchian, Carlos O. S. Sorzano and M. Unser, Fast multiscale reconstruction for Cryo-EM, J. Structural Biology, 204, 3 (2018).

[9] M. Nilchian, J. P. Ward, C.Vonesch and M. Unser, Optimized Kaiser–Bessel Window Functions for Computed Tomography, IEEE Transactions on Image Processing, 24, 11 (2015).

[10] R. M. Lewitt, Multidimensional digital image representations using generalized Kaiser–Bessel window functions, J. Optical Society of America, 7, 10 (1990).

[11] F. Natterer, The mathematics of computerized tomography, Society for Industrial and Applied Mathematics, 2001.

[12] L. I Rudin, S. Osher, and E. Fatemi, Nonlinear total variation based noise removal algorithms, Physica D: nonlinear phenomena, 60, (1992).

[13] X. Qi, P. Schmiege, E. Coutavas, J. Wang and X. Li, Structures of human Patched and its complex with native palmitoylated sonic hedgehog, J. Nature, 560, (2018).

[14] C.O.S. Sorzano, J. Vargas, J. Otón, V. Abrishami, J.M. de la Rosa-Trevín, J. Gómez-Blanco, J.L. Vilas, R. Marabini and J.M. Carazo, A review of resolution measures and related aspects in 3D Electron Microscopy, J. Progress in Biophysics and Molecular Biology, 124, (2017).

[15] E.F. Pettersen, T.D. Goddard, C.C. Huang, G.S. Couch, D.M. Greenblatt, E.C. Meng, and T.E. Ferrin "UCSF Chimera - A Visualization System for Exploratory Research and Analysis." J. Comput. Chem. 25, 13 (2004).

[16] Algorithms for Single Particle Reconstruction (Aspire), http://spr.math.princeton.edu/, Online; accessed 31 January 2019.

JOIN US AT THE NEXT EI!

IS&T International Symposium on

Electronic Imaging

SCIENCE AND TECHNOLOGY

Imaging across applications . . . Where industry and academia meet!

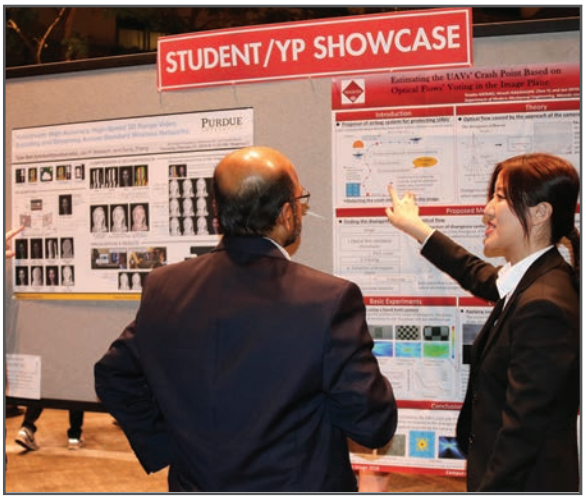

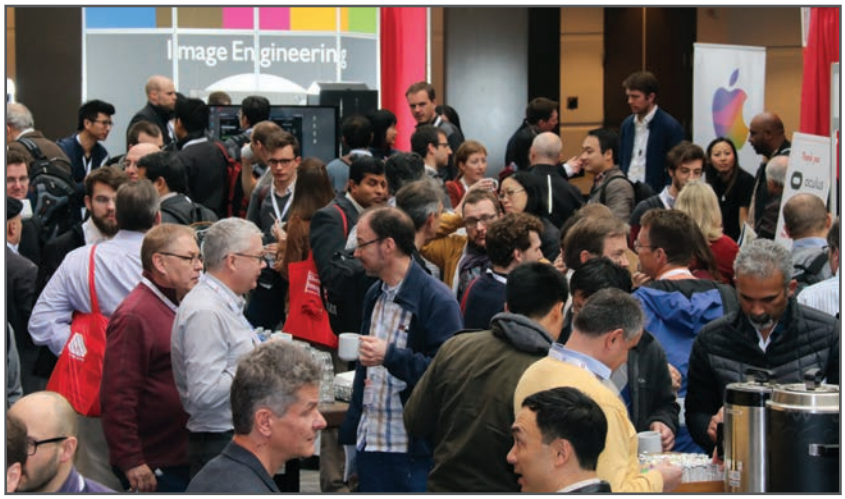

• SHORT COURSES • EXHIBITS • DEMONSTRATION SESSION • PLENARY TALKS •
• INTERACTIVE PAPER SESSION • SPECIAL EVENTS • TECHNICAL SESSIONS •

www.electronicimaging.org

IS&T
imaging.org